PERGAMON

International Journal of Heat and Mass Transfer 44 (2001) 1269–1284

International Journal of HEAT and MASS TRANSFER

www.elsevier.com/locate/ijhmt

Impinging jets confined by a conical wall – high Schmidt mass transfer predictions in laminar flow

João M. Miranda, João B.L.M. Campos *

Centro de Estudos de Fenómenos de Transporte, Departamento de Engenharia Química, Faculdade de Engenharia da Universidade do Porto, 4099 Porto, Portugal

Received 24 November 1999; received in revised form 1 June 2000

Abstract

Mass transfer from a soluble plate to an impinging liquid jet confined by a conical wall is investigated. The nozzle-to-plate distance is very short, less than one nozzle diameter, the flow regime is laminar, $Re < 1600$, and the Schmidt number ranges from 960 to 50 000. Navier–Stokes and solute transport equations are solved by a finite difference scheme. Numerical predictions of the average mass transfer coefficient are compared with data obtained by measuring the dissolution rate of benzoic acid in water and in aqueous solutions of glycerol. A correlation is presented between stagnation Sherwood number, jet Reynolds number and Schmidt number, $Sh_{st}/Sc^{1/3} = 1.77^{1/2}$.

The effects on the mass transfer coefficients of the velocity profile at the nozzle exit and of an insoluble starting length are analyzed. The onset of laminar-to-turbulent transition is identified using mass transfer data. The mass transfer coefficients in the conical cell are compared with those in a radial cell confined by parallel plates.

1. Introduction

Impinging jets are frequently used when high heat and mass transfer rates are required. In industry, they are applied in diverse processes such as in paper and textile drying processes, steel mills, tempering of glass, cooling of turbine blades and electronic components.

The present paper is about mass transfer from a soluble plate placed perpendicular to a laminar impinging jet. The jet flow is confined by a conical wall extending from the nozzle to a short distance above the impingement plate (0.1–0.3 nozzle diameters). The cell is illustrated in Fig. 1, where streamlines representing laminar flow predictions are also shown [1].

The last purpose of the present investigation is to study the applicability of the conical cell to carry out membrane separation processes. In membrane separation studies, mass transfer data for impermeable systems are usually applied to characterize mass transfer rates in the layer adjacent to the porous membrane surface. The present study can be seen as one more step in reaching the final objective; the previous was the study of laminar flow in the conical cell [1].

In the conical cell, the flow field created by an impinging jet is complex, varying from a stagnation type of flow to a wall-jet type of flow. The confinement promotes the development of two recirculation zones, one along the conical wall and another over the impingement plate close to the exit of the cell. Besides this complex flow, the Schmidt numbers of interest are those greater than 960, and so the concentration boundary layer is at least one order of magnitude thinner than the hydrodynamic wall-jet boundary layer. Consequently, a much smaller grid spacing is needed to solve the solute transport equation than to solve the flow equations. These reasons justify the development of a robust numerical procedure, which will be described in detail.

There are few articles published about mass transfer promoted by laminar impinging jets at high Schmidt numbers. Scholz and Trass [2] reported mass transfer data from a flat plate impinged by a free water jet. They

* Corresponding author. Tel.: +351-22-204-1692; fax: +351-22-200-0808.

E-mail address: jmc@fe.up.pt (J.B.L.M. Campos).

0017-9310/01/$ - see front matter
PII: S0017-9310(00)00190-3

Nomenclature

A	surface area of the soluble plate
c	normalized solute concentration (C/C^*)
C	solute concentration
C^*	solute solubility
C_i^1	solute concentration at the outlet of tank i in the inlet pipe of the cell
C_{i-1}^1	solute concentration at the inlet of tank i in the inlet pipe of the cell
C_j^2	solute concentration at the outlet of tank j in the outlet pipe of the cell
C_{j-1}^2	solute concentration at the inlet of tank j in the outlet pipe of the cell
C_0^1	solute concentration in the reservoir and at the reservoir outlet
C_0^2	solute concentration at the cell outlet
C_{M}^2	solute concentration at the reservoir inlet
C_{N}^1	solute concentration at the cell inlet
C_{N}	bulk solute concentration inside the cell
$\mathscr{D}$	solute molecular diffusivity
D_{j}	nozzle (pipe) diameter
D_{p}	impingement plate diameter
h_{s}	normalized height of the sub-domain ($H_{\mathrm{s}}/D_{\mathrm{j}}$)
H	nozzle-to-plate distance
H_{s}	height of the sub-domain
k_r	local mass transfer coefficient
$\bar{k}_r$	average mass transfer coefficient along r
$\bar{k}$	average mass transfer coefficient at the cell exit
L	height of the exit area
$\dot{m}$	mass transfer rate in the cell
M	number of tanks in the outlet pipe of the cell
n	exponent in Eq. (23)
N	number of tanks in the inlet pipe of the cell
Q	liquid flow rate
r	normalized radial coordinate (R/D_{j})
r_0	normalized radial position where the mass boundary layer starts
R	radial coordinate
R_{s}	sum of the total normalized residues of the discretized solute transport equation and boundary conditions or of the flow equations and boundary conditions
t	time
v_{r}	normalized radial velocity ($V_{\mathrm{r}}/V_{\mathrm{j}}$)
v_{z}	normalized axial velocity ($V_{\mathrm{z}}/V_{\mathrm{j}}$)
V_{j}	average jet velocity at the nozzle exit
V_{t}	total volume (reservoir, cell and connecting pipes)
V_0	volume of the reservoir
V^1	volume of each tank in the inlet pipe of the cell
V^2	volume of each tank in the outlet pipe of the cell
z	normalized axial coordinate (Z/D_{j})
Z	axial coordinate

Non-dimensional numbers

Pe	Peclet number ($= D_{\mathrm{j}}V_{\mathrm{j}}/\mathscr{D}$)
Re	Reynolds number based on the jet diameter at the nozzle ($= \rho D_{\mathrm{j}}V_{\mathrm{j}}/\mu$)
Sc	Schmidt number ($= \mu/\rho\mathscr{D}$)
$\overline{Sh}$	average Sherwood number at the cell outlet ($= \bar{k}D_{\mathrm{j}}/\mathscr{D}$)
Sh_r	local Sherwood number ($= k_rD_{\mathrm{j}}/\mathscr{D}$)
$\overline{Sh}_r$	average Sherwood number at r ($= \bar{k}_rD_{\mathrm{j}}/\mathscr{D}$)
Sh_{st}	stagnation Sherwood number ($= k_{r=0}D_{\mathrm{j}}/\mathscr{D}$)

Greek symbols

ρ	liquid density
ω	dimensionless vorticity
ψ	dimensionless stream function
μ	liquid dynamic viscosity

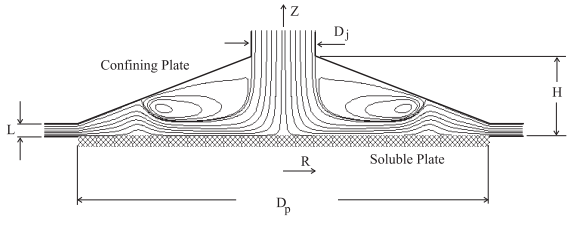

Fig. 1. Cell and laminar flow pattern at $Re = 860$.

determined the local mass transfer coefficients by measuring the decrease in thickness of coatings of acetanilide and benzoic acid and compared the data with the predictions obtained by solving the laminar boundary layer equation along the plate; they observed boundary layer separation and the formation of a toroidal vortex at low jet Reynolds numbers. Chen and Modi [3] numerically studied the mass transfer characteristics of a slot jet impinging normally on a flat wall. This study is for high Schmidt numbers but for turbulent flows. Alkire and Ju [4] also studied the mass transfer characteristics of a slot jet impinging normally on a flat wall, employing an electrochemical technique. They obtained local mass transfer coefficients and developed correlations for three regions along the surface: impingement, transition and wall jet.

There are several studies on heat transfer promoted by laminar impinging jets, but the results can not be extrapolated because, for liquids, the Prandtl number is substantially lower than the Schmidt number. Saad et al. [5] solved the Navier–Stokes and energy equations to predict the flow and the local heat transfer coefficients of a laminar impinging jet confined by an upper plane wall.

They compared their predictions with published data and found a favorable agreement. Elison and Webb [6] studied free-surface and submerged liquid jets impinging perpendicular to a constant heat flux surface for a large range of jet Reynolds numbers. They determined local Nusselt numbers and presented a relationship between stagnation Nusselt number and jet Reynolds number for laminar regimes ($Nu_{st} \propto Re^{0.8}$). Polat et al. [7] published a review article on flow and heat transfer under impinging jets and Jambunathan et al. [8], another one on heat transfer for single circular impinging jets.

1.1. Previous work – laminar flow predictions

Streamlines representing laminar flow predictions are shown in Fig. 1. Miranda and Campos [1] studied the laminar flow in a conical cell and analyzed the effects on the flow pattern of jet Reynolds number, shape of the velocity profile at the nozzle exit and nozzle-to-plate distance. The main conclusions are:

1. The flow inside the cell must be analyzed in three regions: impingement region, wall region and expansion region. At the impingement region, the impinging plate imposes a shift on the fluid direction, which occurs very close to the surface. At the wall region, the fluid flows in a thin channel confined below by the plate and above by fluid in recirculation. At the expansion region, the fluid expands to the whole area of the cell. After the expansion the fluid flows confined by the conical wall and the impingement plate.
2. The jet Reynolds number and the velocity profile at the nozzle exit affect the flow in the entire cell. For low jet Reynolds numbers, the flow direction shifts far from the plate, the upper recirculation zone is radially short and the fluid expands near the axis of the cell. For high jet Reynolds numbers, the flow direction shifts very close to the plate, the upper recirculation zone is radially long, the fluid expands near the exit of the cell and a second recirculation zone appears in the expansion region, close to the plate. If the velocity profile at the nozzle exit is uniform, instead of being parabolic, the flow direction shifts further from the plate, the fluid flows in a thick channel along the wall region and the second recirculation zone does not develop. The nozzle-to-plate distance only affects the flow at the expansion region. When this distance increases, the second recirculation zone enlarges and develops very close to the exit of the cell.
3. The laminar-to-turbulent transition occurs at a critical jet Reynolds number near 1600.
4. The effect of the conical confinement is felt on the radial extension of both recirculation zones; for the same jet Reynolds number and the same nozzle-to-plate distance, the recirculation zones are longer when the confinement is done by parallel plates. The conical wall has a stabilizing effect on the flow, preventing burst of the recirculation zones through the exit of the cell.

The experimental technique is presented in the next section, followed by a description of the numerical work. Afterwards, experimental and numerical data are compared and the results are discussed.

2. Experimental work

2.1. Experimental setup

The experimental setup is shown in Fig. 2. Liquid flowing in a closed circuit was pumped from the reservoir (3) to the cell (1) and returned to the reservoir. The pipe connecting the pump (2) to the cell was long enough to guarantee a well-established laminar flow at the cell inlet. The pump had incorporated an electric heater (12) and a thermocouple (11) and acted as a temperature controller. The liquid in the reservoir was agitated by an impeller (9) driven by an electric motor.

The solute concentration in the reservoir was continuously measured; a small amount of liquid was continuously taken from the reservoir by a high speed peristaltic pump (4), and was analyzed in a spectrophotometer (5) placed in the line. The spectrophotometer was connected to a computer (6) by an RS 232 connecting cable (10) for data acquisition.

The liquid was distilled water or aqueous solutions of glycerol and the solute was benzoic acid. The liquid flow rate was controlled by a metering valve (7) placed in the feed line and was measured by a calibrated rotameter (8).

Spectrophotometric calibration curves were performed for each liquid tested. Linear relationships were

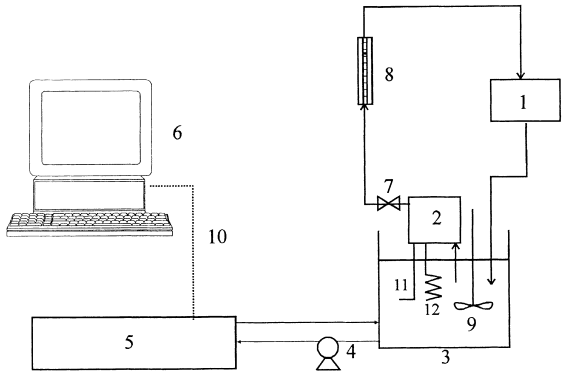

Fig. 2. Experimental setup. Legend: 1 – cell, 2 – pump, 3 – reservoir, 4 – peristaltic pump, 5 – spectrophotometer, 6 – computer, 7 – metering valve, 8 – rotameter, 9 – impeller, 10 – RS 232 connecting cable, 11 – thermocouple and 12 – electric heater.

obtained in a concentration range with an upper limit around 0.5% of benzoic acid solubility.

2.2. Experimental test cell

A front view of the cell, made of brass, is shown in Fig. 3. There is an important constructive detail that must be described: when both parts of the test section (A and B) were set together and the screws were tightened, the o-ring signalized in Fig. 3 was compressed until the stoppers stroked against each other. When they stroked, the distance L shown in Fig. 1 was exactly 1.1 mm. This distance was confirmed by covering all the inner surface of part B with a layer of moldable plastic material. Parts A and B were set together; later they were separated and the measured height of the plastic material was 1.1 mm. At the bottom of the cell, an opening was drilled to make mould removal easier.

The diameter of the inlet pipe was $D_j = 11.7$ mm, that of the impingement plate $D_p = 77.1$ mm and the distance from the nozzle to the plate was $H = 7.7$ mm.

2.3. Mould and soluble plate manufacture

The moulds were made of stainless steel of 90 mm external diameter and 20 mm height. The inner diameter was the pretended for the soluble plate; 10 moulds were assembled with different inner diameters, from 10 to 77.1 mm. A circular section could be adapted to the central part of the mould to manufacture a circular crown of soluble material.

The soluble plate was manufactured by heating the benzoic acid to its melting point. The mould was placed upside down, over a flat metal sheet, and the liquid acid poured through an opening in the base of the mould. The weight of the mould was such that a good seal between the mould and the metal sheet was obtained. The acid was cooled to ambient temperature, and the metal sheet was withdrawn without any damage to the surface of the soluble plate.

2.4. Experimental data treatment

A schematic representation of the closed circuit of the liquid is shown in Fig. 4. The liquid in the reservoir was mixed well. The inlet and outlet solute concentrations, C^2_M and C^1_0, respectively, are related by the following mass balance

$$C^2_M = C^1_0 + \frac{V_0}{Q}\frac{dC^1_0}{dt}, \tag{1}$$

where V_0 is the reservoir volume, and Q is the liquid volumetric flow rate.

The flow along the connecting pipes promotes high solute axial dispersion, particularly when the regime is laminar and the pipes are long – conditions observed in the test-section. The solute dispersion in the connecting pipes was accounted for by the so-called tanks-in-series model [9]. Mass balances to well-mixed tanks of volume V^1, representing the flow in the inlet pipe of the cell, are given by

$$C^1_{i-1} = C^1_i + \frac{V^1}{Q}\frac{dC^1_i}{dt}, \quad i = 1,\ldots,N, \tag{2}$$

where the concentration notation is shown in Fig. 4 and N ranges from 1 (well-mixed flow) to ∞ (plug flow).

Mass balances to well-mixed tanks of volume V^2, representing the flow in the outlet pipe of the cell, are given by

$$C^2_{j-1} = C^2_j + \frac{V^2}{Q}\frac{dC^2_j}{dt}, \quad j = 1,\ldots,M, \tag{3}$$

where the concentration notation is also shown in Fig. 4 and M ranges from 1 (well-mixed flow) to ∞ (plug flow).

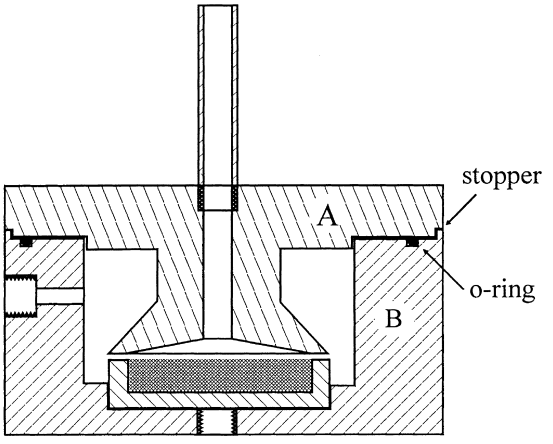

Fig. 3. Front view of the test cell.

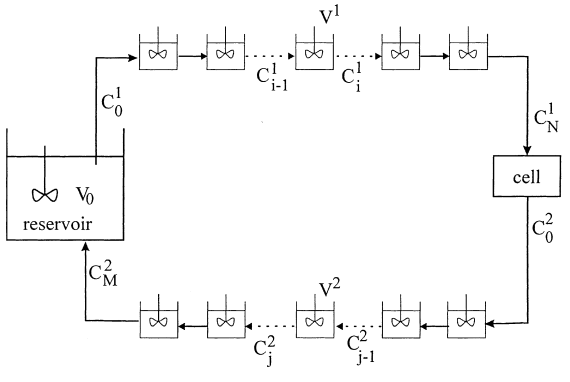

Fig. 4. Schematic representation of the closed circuit of the liquid.

The solute concentrations at the cell inlet and outlet and the mass transfer rate from the soluble plate to the flowing liquid, $\dot{m}$ are related by the following mass balance

$$QC_0^2 = QC_N^1 + \dot{m}. \tag{4}$$

The increasing rate of solute concentration in the reservoir and the mass transfer rate from the soluble plate can be combined through the previous mass balances, Eqs. (1)–(4). By applying Laplace transforms, admitting zero solute concentration in all the circuit at $t = 0$ and considering the theorem of the final value, a relationship between dC_0^1/dt and $\dot{m}$ is established

$$\lim_{t\to\infty} \frac{dC_0^1}{dt} = \frac{\dot{m}}{V_t} \rightarrow V_t \frac{dC_0^1}{dt} = \dot{m}, \tag{5}$$

where V_t is the liquid volume inside the closed circuit: reservoir, connecting pipes and cell.

Following the definition of mass transfer coefficient, the transfer rate $\dot{m}$ and the solute concentration driving force are related by

$$\dot{m} = \bar{k}A(C^* - C_N), \tag{6}$$

where C^* is the equilibrium concentration observed at the plate surface (solubility), A the surface area of the soluble plate, $\bar{k}$ the average mass transfer coefficient and C_N is the bulk solute concentration.

The maximum concentration allowed in the reservoir was 0.5% of the solute solubility (upper limit of the calibration curve). Therefore, the concentration driving force in the cell, $C^* - C_N \approx C^*$, and, according to Eq. (6), the mass transfer rate, $\dot{m}$, were approximately constant along each test-run.

According to Eq. (5), if $\dot{m}$ is constant the increasing rate of C_0^1 must also be so. In Fig. 5 are presented concentration records for three different volumes of liquid in the circuit ($Re = 1050$ and $Sc = 960$). Analyzing record B, an initial abrupt increase of C_0^1 corresponding to the non-stationary start of the test and, as expected, a linear increase from a given instant onwards are observed. The slope of the straight line is $dC_0^1/dt = \dot{m}/V_t$ and the average mass transfer coefficient is given by Eq. (6).

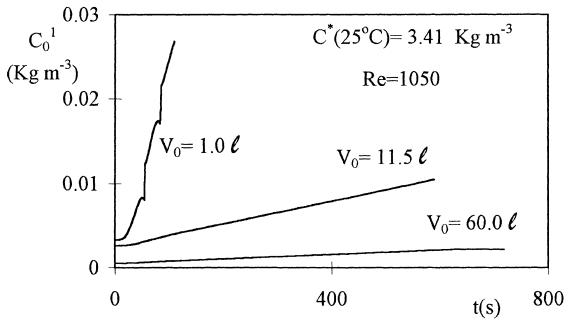

Fig. 5. The evolution of the solute concentration in the reservoir for three total volumes of liquid in the circuit at $Re = 1050$ and $Sc = 960$: A – $V_t = 1$ l, B – $V_t = 11.5$ l, C – $V_t = 60$ l.

Concentration records A and C are to illustrate the preliminary tests done to determine the suitable total volume of liquid in the closed circuit. When this volume is too small (record A), the limit concentration is reached in a very short time, sometimes before the start of the steady state. When this volume is too high (record C), the slope of the straight line, obtained by applying a linear regression to experimental data, is very low and the experimental errors can induce an appreciable uncertainty in the slope value.

Most of the time, several tests were done in a sequential way, with the same solube plate and in the same experimental conditions, until the maximum concentration (0.5% of the solute solubility) in the reservoir was reached. The results of these tests were reproducible with a maximum deviation of the order of the experimental uncertainty. This behavior was important to show that, during each test, the surface shape did not change sufficiently to modify the mass transfer coefficients. The surface of the soluble plate was examined after each series of tests. Sometimes its thickness was measured along the surface, and any significant change in surface shape was detected.

2.5. Experimental mass transfer coefficients

Three distinct mass transfer studies were done with the experimental method earlier described:

1. The average mass transfer coefficient in the cell, $\bar{k}$, was obtained by performing tests with soluble plates of 77.1 mm diameter. For the cell geometry, the objective was to find a relationship between the following non-dimensional numbers: $\overline{Sh}$, Re and Sc.
2. The average mass transfer coefficient along the radius of the cell, $\bar{k}_r$, was obtained by performing tests with soluble plates of different diameters from 10 to 77.1 mm. The objective was to study the evolution of $\overline{Sh}_r$ along r for a given Sc (water–benzoic acid system) and different Re.
3. The effects of an insoluble starting length on the average mass transfer coefficients were also investigated. This was done by comparing the values of average mass transfer coefficients obtained with soluble circular crowns of different inner diameters.

The Schmidt number values ranged from 960 to 50 000, depending on the glycerol concentration in the aqueous solution, and the jet Reynolds number values from 100 to 1600, with the upper limit imposed by the laminar–turbulent transition. The density and dynamic viscosity of the fluids were measured, while the solubility and molecular diffusivity of benzoic acid in water and in aqueous solutions of glycerol were obtained from liter-

ature. The molecular diffusivity of benzoic acid in aqueous solutions of glycerol was obtained from [10], the molecular diffusivity of benzoic acid in water from [11] and the solubility of benzoic acid from [12].

The experimental uncertainty was estimated employing established techniques. The uncertainty in the values of the slopes (calibration curve and dC_0^1/dt) was determined following the methodologies presented in [13] and [14].

For a given Schmidt number, the relative uncertainty in the values of $\overline{Sh}_r$ and $\overline{Sh}$ changes from point to point, along r (Fig. 12(b)) and Re (Fig. 13), respectively. This behavior has much to do with the liquid volume in the circuit (different from experiment to experiment) and with the number of data taken to do the linear regressions. The relative uncertainty in the values of $\overline{Sh}$ increases with Schmidt number (Fig. 13), probably due to fluctuations in the operation temperature and due to lesser solute mixing degree in the reservoir. The maximum relative uncertainty was about 5% for experiments with water and about 7% for experiments with highly viscous glycerol solutions.

3. Numerical study

3.1. Flow equations

The flow equations are written below in the stream function–vorticity formulation. The coordinates are normalized by the nozzle diameter, D_j, the velocity components are normalized by the average jet velocity at the nozzle exit, V_j, and Re represents the jet Reynolds number.

$$\omega r = \frac{\partial^2 \psi}{\partial z^2} - \frac{1}{r}\frac{\partial \psi}{\partial r} + \frac{\partial^2 \psi}{\partial r^2}, \tag{7}$$

$$v_r \frac{\partial \omega}{\partial r} + v_z \frac{\partial \omega}{\partial z} - \omega \frac{v_r}{r} = \frac{1}{Re}\left(\frac{\partial^2 \omega}{\partial r^2} - \frac{\omega}{r^2} + \frac{1}{r}\frac{\partial \omega}{\partial r} + \frac{\partial^2 \omega}{\partial z^2}\right). \tag{8}$$

Eq. (7) is a Poisson-type equation and Eq. (8) is the so-called vorticity transport equation. The dimensionless vorticity ω and stream function ψ are defined as:

$$\omega = \frac{\partial v_r}{\partial z} - \frac{\partial v_z}{\partial r}, \tag{9}$$

$$v_z = -\frac{1}{r}\frac{\partial \psi}{\partial r}; \qquad v_r = \frac{1}{r}\frac{\partial \psi}{\partial z}. \tag{10}$$

3.2. Solute transport equation

The solute transport equation is written below in polar coordinates. The solute concentration is normalized by the solute equilibrium concentration C^*, and Pe represents the Peclet number, $Pe = ReSc = V_j D_j/\mathscr{D}$.

$$v_r \frac{\partial c}{\partial r} + v_z \frac{\partial c}{\partial z} = \frac{1}{Pe}\left(\frac{\partial^2 c}{\partial r^2} + \frac{\partial^2 c}{\partial z^2} + \frac{1}{r}\frac{\partial c}{\partial r}\right). \tag{11}$$

Eqs. (7)–(11) are written assuming laminar and incompressible flow, constant fluid properties and no buoyancy effects.

3.3. Numerical procedure

The mass boundary layer in a liquid-soluble solid contact is very thin and a very refined grid must be employed near the plate to obtain accurate concentration profiles. The solution of the flow and solute transport equations in the numerical domain of the cell, employing the grid used by Miranda and Campos [1] but refined near the soluble plate, was a time consuming task. A numerical strategy was outlined, based on the fact that the solute concentration is different from zero only in a very thin layer near the plate. This numerical strategy involves three steps:

Step I. The solution of the flow equations in the numerical domain of the cell using the grid and the numerical procedure described in [1].

Step II. The solution of the flow equations in a sub-domain near the plate, using a refined and orthogonal grid.

Step III. The solution of the solute transport equation in this sub-domain.

Miranda and Campos [1] solved the flow equations and respective boundary conditions in the numerical domain of the cell by applying a finite difference technique. The numerical domain was not rectangular and a non-orthogonal boundary-fitted grid was used. An algebraic transformation was applied to solve the flow equations in the grid coordinates. The equations were discretized by second-order accurate schemes, and the solution accuracy was studied from solutions on successively refined grids. The rms error defined by Fletcher [15] was always less than 0.02 for the grid employed to predict the flow inside the cell. The effect on the flow of a developing laminar profile at the cell inlet was studied. Therefore, solutions of the flow equations for different inlet velocity profiles were obtained, from uniform to parabolic. For more details see [1].

3.4. Sub-domain and grid

The sub-domain is represented in Fig. 6, and the normalized height of the sub-domain, $h_s = H_s/D_j$, is equal to or less than L/D_j. The grid is shown in Fig. 7 and is orthogonal and non-uniform: (1) the vertical lines are those used to obtain the flow solution in the cell (Step I); (2) the distribution of the horizontal lines is

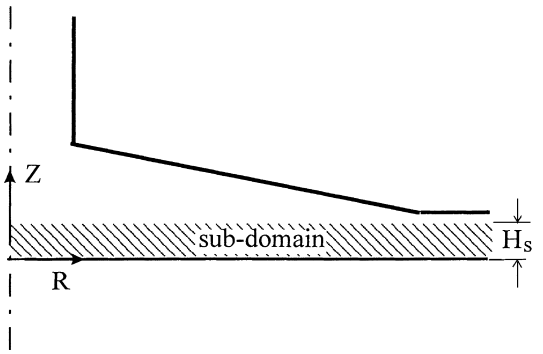

Fig. 6. Numerical sub-domain.

denser near the plate where concentration gradients are high.

3.5. Boundary conditions

The sub-domain and the respective boundaries are represented in Figs. 6 and 7. The elliptic nature of the mass transport equation requires the specification of the boundary conditions at all sides of the numerical sub-domain.

Boundary I. The vorticity and stream function values are obtained by applying linear interpolations to the results of Step I.

As stated earlier, the mass boundary layer is very thin and so either it must be contained in the sub-domain or at least a very small variation of the solute concentration along z must be observed at the boundary, that is

$$\frac{\partial^2 c}{\partial z^2} = 0. \tag{12}$$

This boundary condition was tested by solving the flow and solute transport equations in sub-domains with different normalized heights, $h_s = L/D_j$ and $1/2(L/D_j)$. The predicted concentration profiles were the same and boundary condition (12) was taken to be accurate.

Boundary II. There are no momentum and mass fluxes through the axis of the cell,

$$v_r = 0; \qquad \frac{\partial v_z}{\partial r} = 0; \qquad \psi = 0;$$
$$\omega = 0 \quad \text{and} \quad \frac{\partial c}{\partial r} = 0, \tag{13}$$

Boundary III. At the soluble plate, the no-slip condition is observed

$$v_r = 0; \qquad v_z = 0; \qquad \psi = 0; \qquad \omega = \frac{\partial v_r}{\partial z} \tag{14}$$

and the solute concentration is the solute solubility, $c = 1$.

Boundary IV. The exit is located sufficiently far from the zone of interest, allowing for the application of a condition of developed flow parallel to the impingement plate, which has no upstream influence. Thus,

$$v_z = 0; \qquad \frac{\partial \omega}{\partial r} = -\frac{\omega}{r}; \qquad \frac{\partial \psi}{\partial r} = 0. \tag{15}$$

The developed flow and the low molecular diffusivity of the solute allow for the application of a condition of developed concentration profile, which has no upstream influence. Thus,

$$\frac{\partial c}{\partial r} = 0. \tag{16}$$

3.6. Discretization and solution of the flow equations

The flow equations were discretized by applying a finite difference technique. In the Poisson-type equation, the derivatives were approximated by a second-order accurate central difference scheme. For each node inside the sub-domain, an equation of the following form was obtained

$$r_{i,j}\omega_{i,j} = A_1\psi_{i-1,j} + A_2\psi_{i+1,j} + A_3\psi_{i,j} + A_4\psi_{i,j-1} + A_5\psi_{i,j+1}, \tag{17}$$

where the coefficients A_1–A_5 are shown in Appendix A.

The derivatives in the stream-function boundary conditions were approximated by forward or backward difference, with an accuracy of second order, always in the inward cell direction. For each node an equation of the following form was obtained

$$B_1\psi_{i-2,j} + B_2\psi_{i-1,j} + B_3\psi_{i,j} = b, \tag{18}$$

where the coefficients B_1–B_3 and b are listed in Appendix A.

The vorticity transport equation was discretized by applying an upwind scheme: the derivatives of the diffusive terms were approximated by central difference (accuracy of second order) and the derivatives of the convective terms by forward or backward difference (accuracy of first order). For each node inside the sub-domain, an equation of the following form was obtained

$$D_1\omega_{i-1,j} + D_2\omega_{i+1,j} + D_3\omega_{i,j} + D_4\omega_{i,j-1} + D_5\omega_{i,j+1} = 0, \tag{19}$$

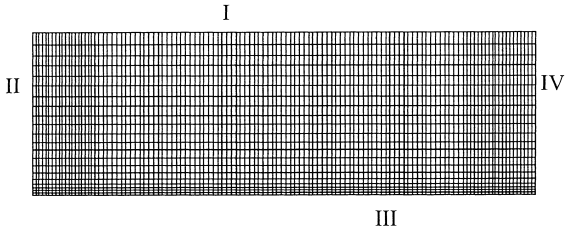

Fig. 7. Grid and boundaries of the sub-domain.

where the coefficients D_1–D_5 are shown in Appendix A.

The vorticity boundary conditions were discretized by applying an identical scheme to that of the stream-function boundary conditions. For each node, an equation of the following form was obtained

$$E_1\omega_{i-2,j} + E_2\omega_{i-1,j} + E_3\omega_{i,j} = e, \tag{20}$$

where the coefficients E_1–E_3 and e are listed in Appendix A.

After discretization, two sets of interrelated algebraic equations were obtained. One set arose from the discretization of the Poisson equation and stream-function boundary conditions and the other set from the discretization of the vorticity transport equation and vorticity boundary conditions. They were solved by an iterative procedure, and in each step, both sets of equations were solved by the alternating direction implicit (ADI) method.

The convergence of the iterative procedure was studied according to the criterion established by [1]; the iterative process was completed when, during one hundred iterations, the absolute difference between consecutive values of v_r (in all the nodes) was less than 10^{-5} and the value of R_s (total normalized residues of the flow equations and boundary conditions) was also less than 10^{-5}.

The accuracy of the numerical method was determined from solutions on successively refined grids; this refinement was done by halving the mesh dimensions of the previous grid. The rms error [15] was computed for these successively refined grids

$$\mathrm{rms} = \left[\left(\sum_{i=1}^{m}\sum_{j=1}^{n_i}\left(v^*_{i,j} - v_{i,j}\right)^2\right)\Big/ p\right]^{1/2}, \tag{21}$$

where starred and non-starred values represent quantities calculated with grids having p^* and p number of nodes, respectively. An identical equation could be written for v_z.

Three tests were performed to study the solution accuracy. The respective grids used and the values of rms found are shown in Table 1. The values of v_r and v_z taken for reference were those obtained with the finest grid. The schemes used in the discretization of the flow equations were of first and second order and, therefore, when the grid spacing is halved, the new value of rms is expected to be about 2–4 times lower than the previous one. Table 1 shows that the ratios between consecutive rms values are of this order of magnitude, and so it is reasonable to infer that the solution of the algebraic flow equations converges to the exact solution. The grid chosen to predict the flow is that in the third line of the table, and the respective flow solution, at $Re = 685$, has rms errors lower than 0.01.

Table 1
Results of the accuracy tests at $Re = 685$ and $Sc = 50000$

	Grid nodes		rms		
	r	z	v_r	v_z	c
A	31	61	0.200	0.022	0.240
B	61	121	0.050	0.006	0.051
C	121	241	0.007	0.0012	0.023
D	241	481	Reference	Reference	Reference

3.7. Discretization and solution of the solute transport equation

The solute transport equation was also discretized by applying an upwind scheme; the derivatives of the diffusive terms were approximated by central difference (accuracy of second order) and the derivatives of the convective terms by forward or backward difference (accuracy of first order). For each node inside the subdomain, an equation of the following form was obtained

$$F_1c_{i-1,j} + F_2c_{i+1,j} + F_3c_{i,j} + F_4c_{i,j-1} + F_5c_{i,j+1} = 0, \tag{22}$$

where the coefficients F_1–F_5 are shown in Appendix A.

At the boundaries, the derivatives were approximated by forward or backward difference, with an accuracy of second order, always in the inward cell direction. For each node in the boundary, an equation of the following form was obtained

$$G_1c_{i-2,j} + G_2c_{i-1,j} + G_3c_{i,j} + G_4c_{i+1,j} + G_5c_{i+2,j} + G_6c_{i,j-2} + G_7c_{i,j-1} = g, \tag{23}$$

where the coefficients G_1–G_7 and g are listed in Appendix A.

After discretization, one set of algebraic equations was obtained and solved by the ADI method. The convergence of the iterative process was studied by analyzing the evolution of the solute concentration in a region where the convergence rate was slow and also by analyzing the sum of the total normalized residues of the solute transport equation and boundary conditions (sum represented by R_s). These procedures are described in [1].

In Fig. 8, the solute concentration evolution along the iterative process at a point located near the end of the soluble plate, at $Re = 685$ and $Sc = 960$, is represented. The values of c converge asymptotically to a constant value, c^∞. After the 275th iteration the absolute difference $|c^\infty - c^{275}|$ is less than 10^{-3} and the absolute difference between consecutive values is less than 10^{-5}. Similar conclusions were obtained regardless of jet Reynolds and Schmidt numbers.

In Fig. 8, the value of R_s along the iterative process at $Re = 685$ and $Sc = 960$ is also represented. There is a decrease in the value of R_s along the process, and after 400 iterations, the value of R_s is three to four orders of magnitude less than that at the begining of the iterative

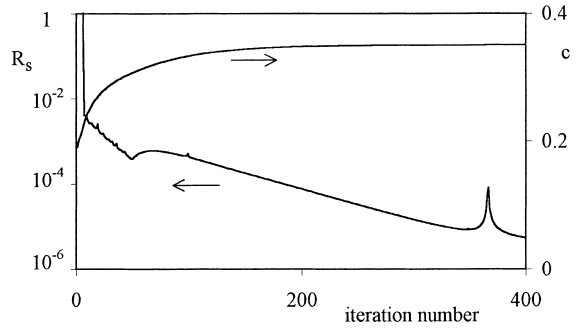

Fig. 8. Evolution along the iterative procedure: (a) solute concentration in a point located near the cell exit; (b) total normalized residues of the solute transport equation and boundary conditions. Both representations are for $Re = 685$ and $Sc = 960$.

process. Once again, similar conclusions were obtained regardless of jet Reynolds and Schmidt numbers.

The fact that, after 400 iterations, the value of c tends towards a stabilized value while R_s is still decreasing confirms the convergence of the iterative method to correct values.

A criterion of convergence was established: the iterative process was completed when, during 50 iterations, the absolute difference between consecutive values of c (in all the nodes) was less than 10^{-5} and the value of R_s was also less than 10^{-5}.

The accuracy of the numerical method was also determined from solutions on successively refined grids. For this purpose, the rms error [15] was applied to normalized solute concentration

$$\mathrm{rms} = \left[\left(\sum_{i=1}^{m} \sum_{j=1}^{n_i} \left(c^*_{i,j} - c_{i,j} \right)^2 \right) \Big/ p \right]^{1/2}. \tag{24}$$

The grids used and the values of rms found are shown in Table 1. The values of c taken for reference were those obtained with the finest grid. The schemes used in the discretization of the solute equation were of first and second order. Table 1 shows that the ratios between consecutive rms values are about 2–4, and so it is reasonable to infer that the solution of the algebraic solute equation converges to the exact solution. The grid chosen to predict the solute distribution is that in the third line of the table, and the respective solution, at $Re = 685$ and $Sc = 50\,000$, has an rms error of the order of 0.023. This value increases with the jet Reynolds number and at $Re = 1685$ it is about 0.035.

The local mass transfer coefficient, k_r,was obtained from the local mass flux

$$k_r = \frac{-\mathscr{D}(\mathrm{d}C/\mathrm{d}z)_{z=0}}{C^*}. \tag{25}$$

As will be shown later, the concentration profiles are linear in the layer adjacent to the plate, and so the derivative in Eq. (25) is given by the slope of the straight line fitting the concentration values in the plate and in the node nearest to the plate.

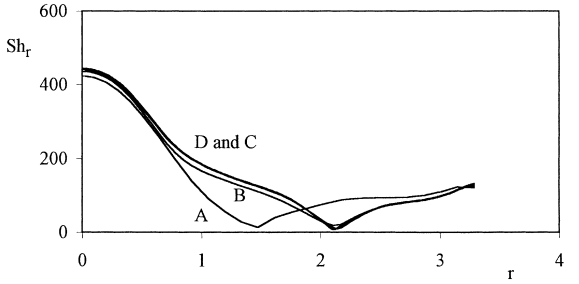

Fig. 9. Local mass transfer coefficients computed with different grid spacing (Table 1), at $Re = 685$ and $Sc = 960$.

The values of k_r, obtained with the grids of Table 1, are plotted along r in Fig. 9 for $Re = 685$ and $Sc = 960$. The similitude between the values predicted with the two last grids of the table proves the accuracy of the solution.

The average mass transfer coefficient, $\bar{k}$, was obtained from the integration of the local mass transfer coefficient along the surface area of the plate

$$\bar{k} = \frac{\int_A k_r \, \mathrm{d}A}{A}. \tag{26}$$

The integral in Eq. (26) was solved numerically by applying the trapezoidal rule, a second-order method.

4. Results

4.1. Flow patterns and mass transfer coefficients

Miranda and Campos [1] concluded that the flow inside the cell must be analyzed in three distinct regions: impingement region, wall region and expansion region. The mass distribution in the vicinity of the soluble plate depends on the flow pattern, and so it should also be analyzed in these regions.

Fig. 10 shows the mass distribution predictions for a water jet ($Sc = 960$) flowing at different jet Reynolds numbers. The several colours correspond to different concentrations according to the legend. The streamlines close to the plate are also represented.

The mass boundary layer thickness is directly related to the competition between the effective axial flux of solute, from the plate towards the bulk of the liquid, and the radial flux of solute, along the plate towards the exit of the cell. If the radial flux is faster than the axial one, the mass boundary layer is thin; otherwise, it is thick. The increase or decrease of the mass boundary layer thickness depends on how this competition occurs along a given length.

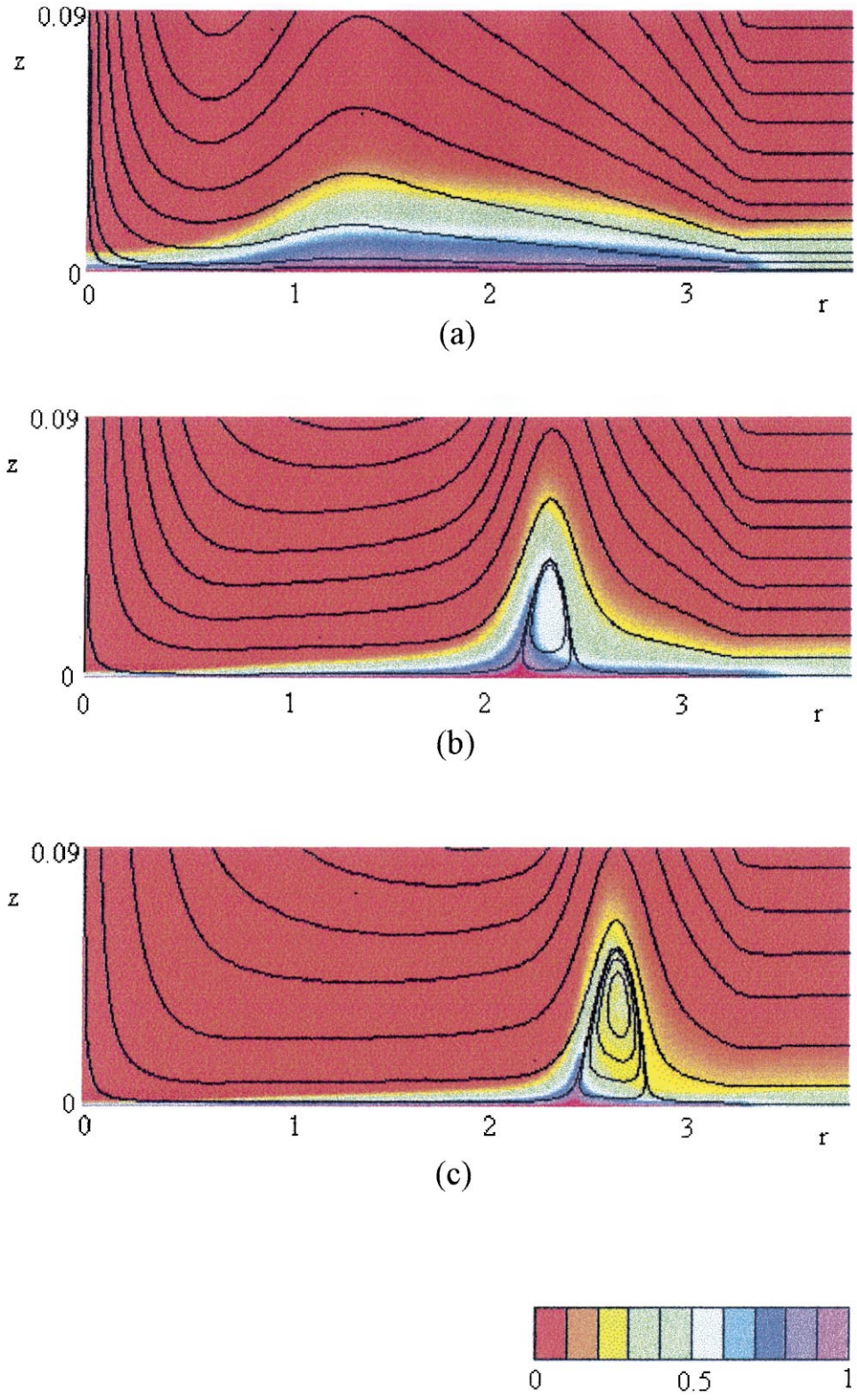

Fig. 10. Mass distribution predictions: (a) $Re = 100$ and $Sc = 960$; (b) $Re = 860$ and $Sc = 960$; (c) $Re = 1685$ and $Sc = 960$.

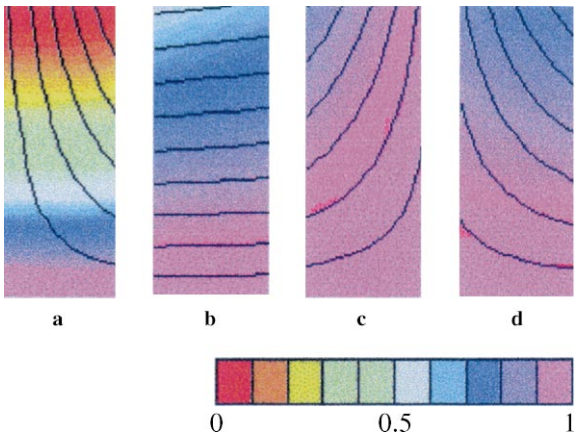

Fig. 11. Flow and the mass distribution inside small control volumes placed over the plate: (a) impingement region; (b) wall region; (c) expansion region; (d) after the expansion region.

At the impingement region, the mass boundary layer is very thin; the thickness is constant near the axis of the cell and begins to increase with the approaching of the wall region. In Fig. 11(a), the streamlines entering and leaving a small control volume placed over the plate and near the axis (in the limit, this volume represents a point near the plate) help in understanding the development of the mass boundary layer in this region. Fresh fluid (without solute) enters through the upper surface of the control volume and hinders solute diffusion in the positive axial direction. This fresh fluid changes direction very close to the plate and the radial momentum increases inside the control volume. The solute radial flux is much faster than the effective axial one, and so the boundary layer is very thin. The axial velocity of the fresh fluid does not change appreciably along the impingement region, and the mass boundary layer thickness remains practically constant.

The axial velocity of the fresh fluid decreases next to the wall region. The axial mass flux acquires importance relative to the radial one and the thickness of the mass boundary layer begins to increase.

At the wall region, the fluid flows radially in a thin channel of almost constant height. The axial momentum diffusion (in the positive direction) induces the exit of fluid with solute through the upper surface of a small control volume taken over the plate (Fig. 11(b)). The radial convective momentum inside the control volume decreases either due to the exit of fluid through the upper surface or due to the increasing cross-sectional area open to the flow (the height of the channel is almost constant and the cross-sectional area increases linearly with r). Along the wall region, the axial convective and diffusive mass fluxes, both in the positive direction, remain practically unchanged, while the radial convective mass flux decreases continuously. Therefore, the thickness of the mass boundary layer grows along this region.

At the fluid expansion, the axial velocity increases abruptly, promoting a strong convective transport of mass in the positive axial direction (Fig. 11(c)). The axial spread of the mass boundary layer is clearly observed in Figs. 10(b) and (c).

After the expansion, the fluid flows towards the exit of the cell. The axial velocity component is in the plate direction, and so fluid with solute enters through the upper surface of a small control volume taken over the plate (Fig. 11(d)). This convective flow hinders solute diffusion in the axial direction and promotes an increase in the radial convective momentum inside the control volume. The radial mass flux becomes important compared to the effective axial flux, and so the thickness of the mass boundary layer decreases along this region.

The extension of the three flow regions depends on jet Reynolds number, and, therefore, the development of the mass boundary layer sustains significant changes along the laminar regime. The mass distribution near the soluble plate for $Re = 100$ is show in Fig. 10(a), and some insights can be had by comparing Figs. 10(a) and (b).

1. The mass boundary layer along the whole plate is thicker for $Re = 100$ than for $Re = 860$. The main reason is that, at the impingement region for $Re = 100$, the fluid changes direction far from the plate, making radial convective mass transport near the plate less intense and less competitive.
2. For $Re = 100$, the extension of the wall region is short, the fluid expansion occurs not far from the cell axis and the mass boundary layer suffers a lesser axial spread during the expansion.

The mass distribution for $Re = 1685$, a value close to the laminar–turbulent transition, is show in Fig. 10(c). The mass transfer process near the recirculation zone located in the vicinity of the impingement plate deserves special attention. The fluid in the outer layers of the recirculation zone flows near the soluble plate during part of the trajectory (part A) and in contact with the fluid flowing around the recirculation zone during the other part (part B). Along part A, the solute concentration in the outer layers increases due to the proximity of the plate. When part B begins, the solute concentration in the outer layers is higher than that in the fluid flowing around and also than that in the fluid recirculating in the inner layers. Therefore, from the outer layers, there is solute transfer in both directions, inwards and outwards. There is a point in part B where the concentration in the outer layers equalizes that in the inner layers but is still higher than that in the fluid flowing around. From there on and until part A, the solute transfer is from the inner layers to the fluid flowing around the recirculation zone. In the steady state, the solute received by the outer layers in part A is lost in part B.

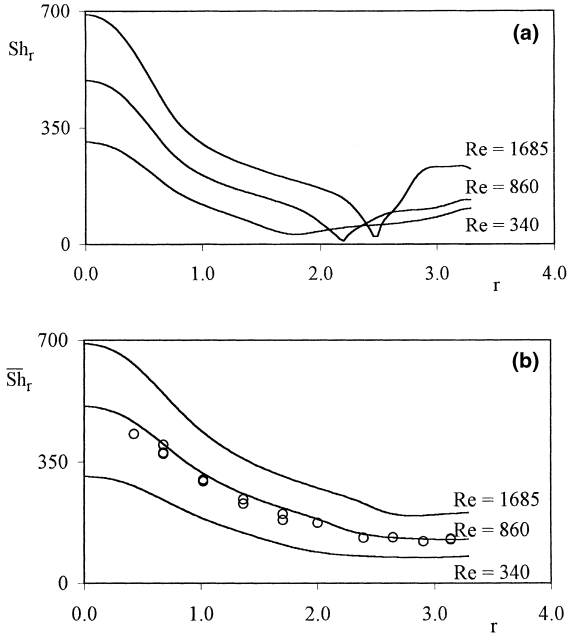

Fig. 12. (a) Sh_r along r for different values of Re at $Sc = 960$; (b) $\overline{Sh}_r$ along r for different values of Re at $Sc = 960$.

Figs. 12(a) and (b) show, respectively, plots of Sh_r and $\overline{Sh}_r$ along r for water jets flowing at different Re; the solid lines represent numerical predictions and the symbols in Fig. 12(b) experimental data. A good agreement between numerical and experimental data can be observed.

The flow effects on the mass boundary layer are also detected from the predictions of the local mass transfer coefficients. At the axis of the cell, Sh_r has its highest value, which remains almost constant during a short distance corresponding to the impingement region length. Along the wall region, the values of Sh_r decrease (the thickness of the mass boundary layer increases), the slope being more pronounced just after the impingement region. When the fluid expands, there is an abrupt decrease and Sh_r reaches its minimum value. After the expansion, there is a gradual increase in the Sh_r values (the thickness of the mass boundary layer decreases gradually).

The curves representing $\overline{Sh}_r$ and Sh_r are similar since $\overline{Sh}_r$ results from the integration of Sh_r along the surface area of the plate. Nevertheless, the curves representing $\overline{Sh}_r$ are smoother, because they are cumulative, and the abrupt changes of Sh_r are attenuated by the sum of the previous values. After fluid expansion, the values of $\overline{Sh}_r$ do not change significantly along r. In Fig. 13, the values of $\overline{Sh}$ versus Re for different values of Sc are plotted; the symbols represent the experimental data and the solid lines the numerical predictions. For each Schmidt number, a data correlation of the form $\overline{Sh} = aRe^b$ has

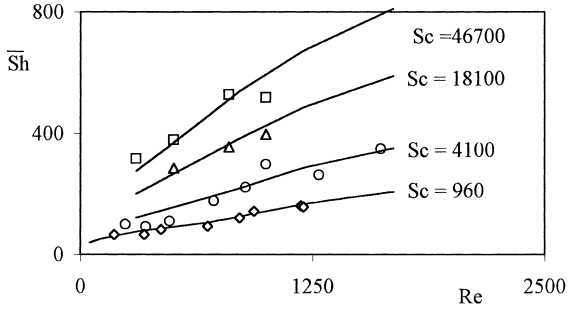

Fig. 13. $\overline{Sh}$ versus Re for different values of Sc.

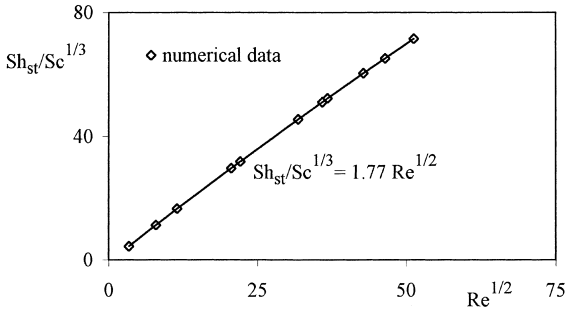

Fig. 14. $Sh_{st}/Sc^{1/3}$ versus $Re^{1/2}$. The symbols represent numerical predictions for $960 < Sc < 50\,000$.

poor significance because the principle of similarity of the flow solution with respect to jet Reynolds number is not observed. This principle is only observed at the cell axis, in the stagnation region. In Fig. 14 $Sh_{st}/Sc^{1/3}$ is plotted versus $Re^{1/2}$, with the constants determined by applying a least-square regression to the numerical data (symbols in the plot). The value 1/2 was expected since it is the value predicted by laminar theory for stagnation flow due to the formation of an initially laminar boundary layer.

4.2. Mass transfer coefficients and Schmidt number

The solution of the solute transport equation depends on the jet Reynolds number and on the Peclet number ($Pe = ReSc$). This last number measures the competition between convective and diffusive mass transport. It is well known that for almost all solid–liquid contact systems, the values of Pe are high, the mass diffusion being limited to a thin layer over the soluble solid. In laminar flow, the limiting case $Pe \to \infty$ was solved for the first time, many years ago, by Leveque [16], who assumed that the entire mass field is confined within a zone where the velocity profile is linear. From then on, the solution of many mass-heat transfer problems dealing with strong convection effects

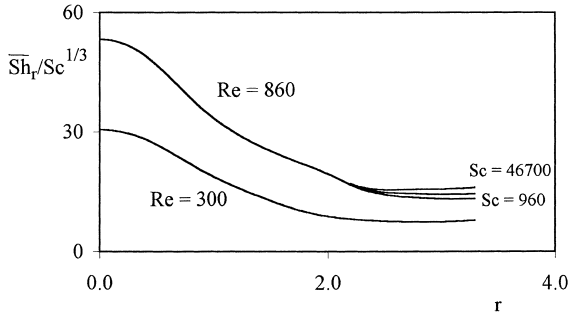

Fig. 15. $\overline{Sh}_r/Sc^{1/3}$ along r at $Re = 300$ and at $Re = 860$ for $960 < Sc < 50\,000$.

in different geometries was based on the previous assumption and all concluded that $Sh(Nu) \propto Pe^{1/3}$.

In the present work, some numerical simulations were performed to study the dependence of $\overline{Sh}_r$ on Sc and the results are plotted in Fig. 15. At $Re = 300$ all the $\overline{Sh}_r/Sc^{1/3}$ values obtained for a large range of Schmidt numbers (from 960 to 50 000) lie on the same curve, but at $Re = 860$ they only lie on the same curve until the beginning of the fluid expansion. This behavior can be explained by analyzing the velocity profiles inside the mass boundary layer; they are linear along the impingement and wall regions, but deviate from linearity at the expansion region, and this deviation is more pronounced for high values of jet Reynolds number.

4.3. The effects of an insoluble starting length

The effect of an insoluble starting length, r_0, on the mass transfer coefficients was numerically and experimentally investigated. In Figs. 16(a) and (b) the values of Sh_r and $\overline{Sh}$ are plotted for different values of r_0 at $Re = 860$ and $Sc = 960$; the solid lines represent numerical predictions and, in Fig. 16(b), the symbols represent experimental data.

If the mass boundary layer starts before the fluid expansion, $r_0 < 2.2$, the values of the local mass transfer coefficient tend towards the same minimum value at $r = 2.2$. After the axial fluid expansion, the concentration profiles near the plate are similar, whatever the values of r_0, and the local mass transfer coefficients have the same value. The expansion acts by "cleaning the history" of the mass boundary layer. If the mass boundary layer starts after the fluid expansion, the values of the local mass transfer coefficient depend on r_0.

The data in Fig. 16(b) complement the previous analysis; the average mass transfer coefficient in the cell does not depend on r_0 if the mass boundary layer starts before the fluid expansion, but if it starts after the fluid expansion, the average mass transfer coefficient in the cell increases with r_0.

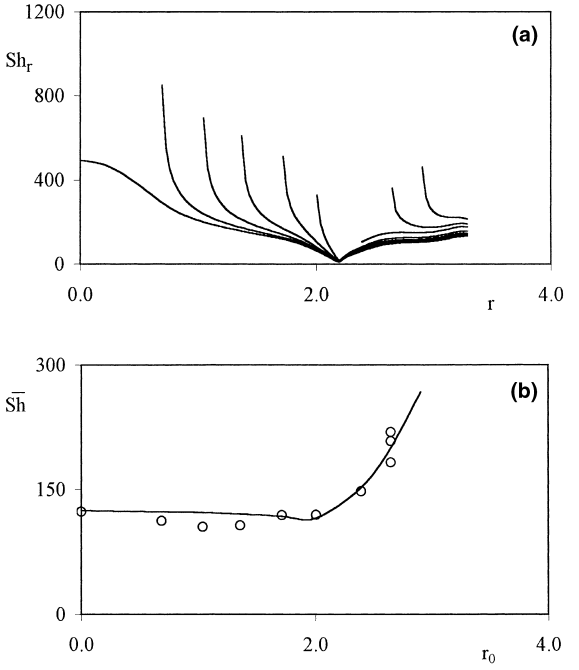

Fig. 16. Insoluble starting length effect: (a) Sh_r along r for different r_0 at $Re = 860$ and $Sc = 960$; (b) $\overline{Sh}$ versus r_0 at $Re = 860$ and $Sc = 960$.

4.4. Mass transfer coefficients and cell geometry

Miranda and Campos [1] compared the radial flows in a conical cell and in a cell with parallel plates. The flow patterns are similar except that, in the parallel confinement, both recirculation zones are more radially extended. When the confinement plates are short, these zones burst through the outflow boundary, leading to an inflow which promotes instability inside the cell. For the dimensions of the cell in the study, nozzle-to-impingement plate distance and ratio between nozzle and impingement plate diameters, the recirculation zone in the vicinity of the impingement plate bursts at an Re around 400.

In Figs. 17(a) and (b), the values of Sh_r and $\overline{Sh}_r$ are compared for both confinements, at $Re = 300$ and $Sc = 960$. The values of Sh_r coincide until fluid expansion occurs in the conical cell ($r = 1.7$), and from there on, the values of Sh_r are higher in the conical confinement. Fig. 17(b) shows that, for the dimensions of the plate in study, the value of $\overline{Sh}$ is about 20% higher when the confinement is done by a conical wall.

4.5. Mass transfer coefficients and inlet velocity profile

In the introduction, it was stated that the velocity profile at the cell inlet determines the flow along the

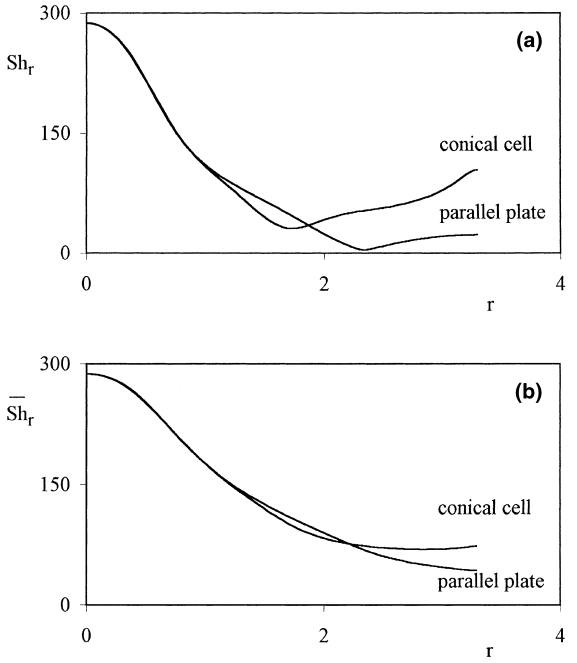

Fig. 17. Comparison between conical and parallel plate confinements: (a) Sh_r along r at $Re = 300$ and $Sc = 960$; (b) $\overline{Sh}_r$ along r at $Re = 300$ and $Sc = 960$.

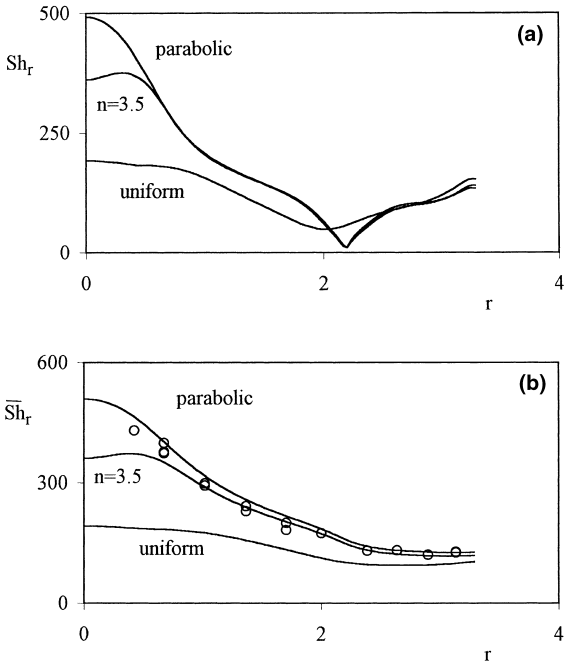

Fig. 18. Importance of the velocity profile at the nozzle exit: (a) Sh_r along r at $Re = 860$ and $Sc = 960$; (b) $\overline{Sh}_r$ along r at $Re = 860$ and $Sc = 960$.

whole cell. According to Miranda and Campos [1], if the velocity profile is uniform, instead of parabolic, the fluid shifts direction further from the plate, and the fluid flows in a thick channel along the wall region. If the flow field is substantially changed, the same must happen to the mass distribution near the soluble surface. Fig. 18(a) shows the Sh_r predictions for $Re = 860$ at $Sc = 960$, assuming different velocity profiles at the cell inlet: parabolic, uniform and a profile pertaining to non-fully developed flow. A normalized developing laminar profile is well represented by

$$v_r = 0; \qquad v_z = -\frac{n+2}{n}[1-(2r)^n], \tag{27}$$

where n ranges from 2 (laminar flow) to ∞ (uniform flow).

Analyzing the curves of Fig. 18(a), one can conclude that: (1) at the impingement region, the Sh_r values are very sensitive to the shape of the inlet velocity profile; (2) along the wall region, there is a convergence of the values obtained with the different inlet velocity profiles. In the cumulative curve represented in Fig. 18(b), the differences between the $\overline{Sh}_r$ values near the axis are attenuated along the radius due to the increasing mass transfer area. The deviation between $\overline{Sh}$ values for a parabolic profile and for a uniform one is of the order of 10%.

4.6. Laminar–turbulent transition

Miranda and Campos [1] studied laminar-to-turbulent transition employing a laser Doppler anemometer to measure the radial velocity component and its fluctuation in several positions along the flow. They concluded that the transition begins at a critical Reynolds number around 1600.

The experimental mass transfer data confirm this value. Fig. 19 shows the radial velocity measured in one point of the flow and also $\overline{Sh}$ experimental data for a large range of Re. In both representations, there is a

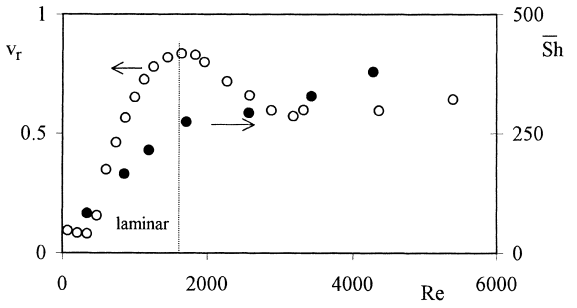

Fig. 19. Laminar-to-turbulent transition. Radial velocity at one point of the flow measured with an LDA system and $\overline{Sh}$, both represented for a large range of Re at $Sc = 960$.

change in behavior at an *Re* around 1600, a clear indication of an alteration of the flow regime.

5. Conclusions

The mass transfer rate from a circular plate into an impinging jet flowing in a conical cell is strongly affected by the liquid flow pattern. The principle of flow similarity with respect to jet Reynolds number is not observed, and so a generic correlation between Sherwood and jet Reynolds numbers has poor physical meaning. This principle is observed at the stagnation region and a correlation $Sh_{st}/Sc^{1/3} = 1.77Re^{1/2}$ was obtained. The values of the exponents were expected: (1) 1/2 is the value predicted by laminar theory for stagnation flow due to the formation of an initially laminar boundary layer; (2) 1/3 is the value predicted when there are strong convection effects and the velocity profile is linear inside the thin mass boundary layer.

The velocity profile is not always linear inside the mass boundary layer; at the expansion region, for high jet Reynolds number, there is a strong axial spread of the mass boundary layer and the velocity profiles near the plate are no longer linear. Therefore, a correlation $\overline{Sh}_r \propto Sc^{1/3}$ has some meaning only for low jet Reynolds numbers, $Re <\approx 300$.

An insoluble starting length, r_0, does not affect the average mass transfer coefficient in the cell if r_0 is less than the radial position where the fluid expansion occurs. However, if the soluble plate begins after the fluid expansion, the average mass transfer coefficients increase with r_0.

For large plates, the average mass transfer coefficient in a conical cell is higher than that in a cell with parallel plates. This conclusion, together with the unstable flow observed in a cell with parallel plates, points out the importance of the conical geometry.

The local mass transfer coefficients in the region near the axis of the cell are strongly affected by the jet velocity profile at the nozzle exit. However, the average coefficients in the cell (for the cell dimensions studied) do not differ very much whatever the shape of the inlet profile (uniform or parabolic).

The mass transfer data confirm the value of 1600 as the critical Reynolds number for the onset of laminar-to-turbulent flow transition.

Acknowledgements

The authors acknowledge the financial support given by JNICT, project PBIC/C/CEN/1337/92 and by F.C.T., PRAXIS XXI/BD/3280/94 and project PRAXIS/C/EQU/12141/1998.

Appendix A

The coefficients of the discretized flow equations, presented in this appendix, are expressed for the node (*i*,*j*) of the grid represented in Fig. 6.

The coefficients of the discretized Poisson equation are computed from the following expressions:

$$A_1 = A_{1,1} + A_{1,2}, \qquad A_2 = \delta_j A_{1,1} - \delta_j^2 A_{1,2},$$
$$A_3 = -(A_1 + A_2 + A_4 + A_5),$$
$$A_4 = \frac{2}{(z_{i,j} - z_{i,j-1})(z_{i,j+1} - z_{i,j-1})} \quad \text{and} \quad A_5 = \varepsilon A_4,$$

where

$$A_{1,1} = \frac{2}{(r_{i,j} - r_{i-1,j})(r_{i+1,j} - r_{i-1,j})},$$

$$A_{1,2} = \frac{r_{i+1,j} - r_{i,j}}{r_{i,j}(r_{i,j} - r_{i-1,j})(r_{i+1,j} - r_{i-1,j})},$$

$$\delta_j = \frac{r_{i,j} - r_{i-1,j}}{r_{i+1,j} - r_{i,j}} \quad \text{and} \quad \varepsilon = \frac{z_{i,j} - z_{i,j-1}}{z_{i,j+1} - z_{i,j}}.$$

The coefficients of the discretized vorticity transport equation are computed from the following expressions

$$D_1 = D_{1,1} + D_{1,2} + D_{1,3},$$

$$D_2 = -\delta_j^2 D_{1,2} + \delta_j D_{1,3} + D_{2,1},$$

$$D_3 = -(D_1 + D_2 + D_4 + D_5) + \frac{1}{Re\, r_{i,j}^2} - \frac{v_{r_{i,j}}}{r_{i,j}},$$

$$D_4 = D_{4,1} + D_{4,2} \quad \text{and} \quad D_5 = C_{5,1} + \varepsilon D_{4,2},$$

where

$$D_{1,1} = \begin{cases} v_{r_{i,j}} > 0 & -\frac{v_{r_{i,j}}}{r_{i,j} - r_{i-1,j}} \\ v_{r_{i,j}} < 0 & 0 \end{cases};$$

$$D_{1,2} = \frac{r_{i+1,j} - r_{i,j}}{r_{i,j}(r_{i,j} - r_{i-1,j})(r_{i+1,j} - r_{i-1,j})Re};$$

$$D_{1,3} = -\frac{2}{(r_{i,j} - r_{i-1,j})(r_{i+1,j} - r_{i-1,j})Re};$$

$$D_{2,1} = \begin{cases} v_{r_{i,j}} > 0 & 0 \\ v_{r_{i,j}} < 0 & \frac{v_{r_{i,j}}}{r_{i+1,j} - r_{i,j}} \end{cases};$$

$$D_{4,1} = \begin{cases} v_{z_{i,j}} > 0 & -\frac{v_{z_{i,j}}}{z_{i,j} - z_{i,j-1}} \\ v_{z_{i,j}} < 0 & 0 \end{cases};$$

$$D_{4,2} = -\frac{2}{(z_{i,j} - z_{i,j-1})(z_{i,j+1} - z_{i,j-1})Re};$$

$$D_{5,1} = \begin{cases} v_{z_{i,j}} > 0 & 0 \\ v_{z_{i,j}} < 0 & \frac{v_{z_{i,j}}}{z_{i,j+1} - z_{i,j}} \end{cases}.$$

The coefficients of the discretized mass transport equation are computed from the following expressions

$$F_1 = F_{1,1} + F_{1,2} + F_{1,3},$$

$$F_2 = -\delta_j^2 F_{1,2} + \delta_j F_{1,3} + F_{2,1},$$

$$F_3 = -(F_1 + F_2 + F_4 + F_5),$$

$$F_4 = F_{4,1} + F_{4,2} \quad \text{and} \quad F_5 = F_{5,1} + \varepsilon F_{4,2},$$

where

$$F_{1,1} = D_{1,1}, \qquad F_{1,2} = \frac{Re}{Pe} D_{1,2}, \qquad F_{1,3} = \frac{Re}{Pe} D_{1,3},$$

$$F_{2,1} = D_{2,1}, \qquad F_{4,1} = D_{4,1}, \qquad F_{4,2} = \frac{Re}{Pe} D_{4,2}$$

and $F_{5,1} = D_{5,1}$.

The coefficients of the boundary equations are computed from the following expressions.

Boundary I

$$G_1 = G_2 = G_4 = G_5 = 0, \qquad G_3 = 1, \qquad g = 0,$$

$$G_6 = \frac{z_{i,j} - z_{i,j-1}}{z_{i,j-1} - z_{i,j-2}}, \qquad G_7 = -\frac{z_{i,j} - z_{i,j-2}}{z_{i,j-1} - z_{i,j-2}}.$$

Boundary II

$$B_1 = B_2 = 0, \qquad B_3 = 1, \qquad b = 0; \qquad E_1 = E_2 = 0,$$

$$E_3 = 1, \qquad e = 0; \qquad G_1 = G_2 = 0, \qquad G_3 = -3,$$

$$G_4 = 4, \qquad G_5 = -1, \qquad G_6 = G_7 = 0 \quad \text{and} \quad g = 0.$$

Boundary III

$$B_1 = B_2 = 0, \qquad B_3 = 1, \qquad b = 0; \qquad E_1 = E_2 = 0,$$

$$E_3 = 1 \qquad e = \frac{(z_{i,j+2} - z_{i,j})^2 v_{r_{i,j+1}} - (z_{i,j+1} - z_{i,j})^2 v_{r_{i,j+2}}}{(z_{i,j+2} - z_{i,j+1})(z_{i,j+2} - z_{i,j})(z_{i,j+1} - z_{i,j})}.$$

Boundary IV

$$B_1 = 1, \qquad B_2 = -4, \qquad B_3 = 3, \qquad b = 0;$$

$$E_1 = 1, \qquad E_2 = -4, \qquad E_3 = 3 + \frac{2\Delta r_j}{r_{i,j}}; \qquad e = 0,$$

with $\Delta r_j = r_{i,j} - r_{i-1,j} = r_{i-1,j} - r_{i-2,j}$;

$$G_1 = 1, \qquad G_2 = -4, \qquad G_3 = 3,$$

$$G_4 = G_5 = G_6 = G_7 = 0 \quad \text{and} \quad g = 0.$$

References

[1] J.M. Miranda, J.B.L.M. Campos, Impinging jets confined by a conical wall – laminar flow predictions, AIChE J. 45 (1999) 2273–2285.

[2] M.T. Scholtz, O. Trass, Mass transfer in the laminar radial wall jet, AIChE J. 9 (1963) 548–554.

[3] Q. Chen, V. Modi, Mass transfer in turbulent impinging slot jets, Int. J. Heat Mass Transfer 42 (1999) 873–887.

[4] R. Alkire, J.-B. Ju, High speed selective electroplating with impinging two-dimensional slot jet flow, J. Electrochem. Soc.: Electrochemical Science and Technology 134 (1987) 294–299.

[5] N.R. Saad, W.J.M. Douglas, A.S. Mujumdar, Prediction of heat transfer under an axisymmetric laminar impinging jet, Ind. Eng. Chem., Fundam. 16 (1977) 148–154.

[6] B. Elison, B.W. Webb, Local heat transfer to impinging liquid jets in the initially laminar, transitional, and turbulent regimes, Int. J. Heat Mass Transfer 37 (1994) 1207–1216.

[7] S. Polat, B. Huang, A.S. Mujumdar, W.J.M. Douglas, Numerical flow and heat transfer under impinging jets: a review, Annu. Rev. Numer. Fluid Mech. Heat Transfer 2 (1989) 157–197.

[8] K. Jambunathan, E. Lai, M.A. Moss, B.L. Button, A review of heat transfer data for single circular jet impingement, Int. J. Heat Fluid Flow 13 (1992) 106–115.

[9] O. Levenspiel, Chemical Reaction Engineering, second ed., Wiley, New York, 1972.

[10] P. Harriott, R.M. Hamilton, Solid–liquid mass transfer in turbulent pipe flow, Chem. Eng. Sc. 20 (1965) 1073–1178.

[11] R.A. Noulty, D.G. Leaist, Diffusion coefficient of aqueous benzoic acid at 25°C, J. Chem. Eng. Data 32 (1987) 418–420.

[12] M. Eisenberg, P. Chang, W.T. Charles, C.R. Wilke, Physical properties of organic acids, AIChE J. 1 (1955) 558.

[13] K.K. Brown, H.W. Coleman, W. Gleen Steele, A methodology for determining experimental uncertainities in regressions, J. Fluids Eng. 120 (1998) 445–456.

[14] J. Mandel, The Statistical Analysis of Experimental Data, Dover, New York, 1964.

[15] C.A.J. Fletcher, Computational Techniques for Fluid Dynamics I, in: Springer Series in Computational Physics, Springer, Berlin, 1988.

[16] M.A. Leveque, Les lois de la transmission de chaleur par convection, Ann. Mines 13 (1928) 201–239.